# AIAA 2003–1097

## AN ITERATIVE DECAMBERING APPROACH FOR POST-STALL PREDICTION OF WING CHARACTERISTICS USING KNOWN SECTION DATA

Rinku Mukherjee, Ashok Gopalarathnam,
*Department of Mechanical and Aerospace Engineering,*
*North Carolina State University, Raleigh, NC 27695-7910*
and
SungWan Kim
*NASA Langley Research Center,*
*Hampton, VA 23681-2199*

**41st AIAA Aerospace Sciences Meeting**
January 6–9, 2003/Reno, Nevada

# AN ITERATIVE DECAMBERING APPROACH FOR POST-STALL PREDICTION OF WING CHARACTERISTICS USING KNOWN SECTION DATA

Rinku Mukherjee,* Ashok Gopalarathnam,†
*Department of Mechanical and Aerospace Engineering,*
*North Carolina State University, Raleigh, NC 27695-7910*
and
SungWan Kim‡
*NASA Langley Research Center,*
*Hampton, VA 23681-2199*

**An iterative decambering approach for the post stall prediction of wings using known section data as inputs is presented. The method can currently be used for incompressible flow and can be extended to compressible subsonic flow using Mach number correction schemes. A detailed discussion of past work on this topic is presented first. Next, an overview of the decambering approach is presented and is illustrated by applying the approach to the prediction of the two-dimensional $C_l$ and $C_m$ curves for an airfoil. The implementation of the approach for iterative decambering of wing sections is then discussed. A novel feature of the current effort is the use of a multidimensional Newton iteration for taking into consideration the coupling between the different sections of the wing. The approach lends itself to implementation in a variety of finite-wing analysis methods such as lifting-line theory, discrete-vortex Weissinger's method, and vortex lattice codes. Results are presented for a rectangular wing for $\alpha$ from 0 to 25 deg. The results are compared for both increasing and decreasing directions of $\alpha$, and they show that a hysteresis loop can be predicted for post-stall angles of attack.**

## Nomenclature

| | |
|---|---|
| $C$ | damping factor |
| $C_L$ | wing lift coefficient |
| $C_l$ | airfoil lift coefficient |
| $C_m$ | airfoil pitching moment coefficient about the quarter chord |
| $c$ | chord |
| $\mathbf{F}$ | residual vector |
| $f$ | element of residual vector |
| $i, j$ | index of wing section |
| $\mathbf{J}$ | Jacobian matrix |
| LLT | lifting line theory |
| $N$ | number of wing sections |
| VLM | vortex lattice method |
| $x_2$ | chordwise start location of the second decambering function |
| $\alpha$ | angle of attack |
| $\beta$ | angle of yaw |
| $\Gamma$ | strength of bound vortex |
| $\delta\mathbf{x}$ | vector containing the corrections to the Newton variables |
| $\delta_1(x)$ | first decambering function |
| $\delta_2(x)$ | second decambering function |
| $\theta_2(x)$ | angular coordinate corresponding to $x_2$ |

**Subscripts**

| | |
|---|---|
| $max$ | maximum |
| $sec$ | represents value for a wing section |
| $visc$ | represents value from two-dimensional viscous experimental or computational data |

## Background and Introduction

With the remarkable success of Prandtl's lifting-line theory (LLT) in being able to predict the flow past medium- to high-aspect ratio unswept wings in incompressible flow, LLT became a standard tool for computing wing aerodynamics. As is well known, LLT uses a single unswept lifting line (or bound vortex) to model the circulation on the wing. The strength of this bound vortex, $\Gamma$, varies along the span. At any given spanwise location, the change in $\Gamma$ is shed as trailing vorticity, which in turn causes induced velocities along the lifting line. LLT enables the computation of the $\Gamma$ distribution for which the accompanying induced velocities and the resulting effective angles of attack along the span support the $\Gamma$ distribution. For this purpose, the classical Prandtl LLT assumes a linear lift-curve slope for the airfoil sections that form the wing. This lift-curve slope is typically close to $2\pi$ per radian.

*Graduate Research Assistant, Box 7910, Student Member, AIAA. e-mail: rmukher@eos.ncsu.edu. Research supported by Grant NAG-1-01119 from the NASA Langley Research Center.

†Assistant Professor, Box 7910, (919) 515-5669. Member, AIAA. e-mail: ashok_g@ncsu.edu Research supported by Grant NAG-1-01119 from the NASA Langley Research Center.

‡Research Engineer, Associate Fellow, AIAA. e-mail:s.kim@larc.nasa.gov

With the success of LLT in the prediction of wing flows at low angles of attack, the attention soon turned to whether LLT could be modified for the analysis of wings where nonlinear lift-curve slopes for the airfoil sections can be taken into consideration. The motivation was provided by the fact that the airfoil lift curve often deviates from the linear curve due to separation as the angle of attack approaches stall. Tani[1] is believed to have developed the first successful technique in 1934 for handling nonlinear section lift-curve slopes in the LLT formulation. In his technique, a spanwise bound vorticity ($\Gamma$) distribution is first assumed; this distribution is used to compute the distribution of induced velocities and hence induced angles and effective angles of attack along the lifting line. The distribution of effective angle of attack is then used to look up the operating $C_l$ of the local section using the known nonlinear $C_l$-$\alpha$ data for the airfoil. A new $\Gamma$ distribution is then computed from the spanwise $C_l$ distribution. The iteration is carried out until the $\Gamma$ distribution converges. This method was made popular by the NACA report of Sivells and Neely[2] in 1947 that provides a detailed description of the method and implements a tabular procedure for hand-calculation of the method for unswept wings with arbitrary planform and airfoil lift-curve slopes. In Ref. 2, this method was applied for analysis of wings up to the onset of stall, i.e., until a wing angle of attack at which some section on the wing has $C_l$ equal to the local section $C_{l_{max}}$. At higher angles of attack, where some sections on the wing may have a negative lift-curve slope, this successive approximation approach appears to have failed.

According to Sears,[3] Von Kármán noticed that Prandtl's lifting-line equation has nonunique solutions for cases when the lift-curve slope becomes negative (i.e. when the $\alpha$ increases past the onset of stall). These nonunique solutions include both symmetrical and antisymmetric lift distributions even when the geometry and onset flow are both symmetric. Sears[3] mentions that Von Kármán further postulated that even in the conditions just past the onset of wing stall, when some sections of the wing may have positive lift-curve slopes (pre-stall condition) and other sections may have negative lift-curve slopes (post-stall condition), nonunique and asymmetric lift distributions are possible. It occurred to Von Kármán and Sears that the appearance of large and sometimes violent rolling moments past stall on symmetric wind-tunnel models at zero yaw may be explained by the possibility of asymmetric lift distributions at perfectly symmetric flight conditions.

The investigation suggested by Von Kármán on computing the symmetric and asymmetric lift distributions on wings operating beyond stall was carried out and was reported in a 1939 thesis[4] by Schairer working under the supervision of Sears. Schairer apparently used the same procedure as that pioneered by Tani, but had to use a tedious trial-and-error procedure to find the solutions as Tani's successive-approximation procedure failed to work for these partially-stalled cases. Sears[3] presents some of Schairer's results for a flat, untwisted elliptic wing of aspect ratio 10.19 operating beyond stall. The results show solutions consisting of asymmetric lift distributions (in addition to a classical symmetric solution) with large associated rolling moments for a narrow range of angles of attack just beyond stall. Sears mentions that the choice between the symmetric and asymmetrical solution would require the formidable solution of the relative stability of the two flows. Sears concludes by pointing out the need for further progress on the analysis of wings at near- and post-stall conditions.

Piszkin and Levinsky[5] developed a nonlinear lifting line method based in part on the iterative method originally conceived by Tani.[1] As described in Ref. 6, they were motivated by the need for a method that could predict adverse wing stalling characteristics such as wing drop, loss of roll control and roll control reversal at zero yaw. These characteristics were believed to be caused by the occurrence of asymmetric lift distributions on wings with stalled or partially-stalled flow.

The method of Piszkin and Levinsky utilizes a finite element, unsteady wake, incompressible flow theory that can be used for analysis at either zero or nonzero yaw. The model uses a single chordwise row of horseshoe vortices distributed along the span, with the bound vortex aligned with the local quarter-chord line. The boundary condition of zero normal flow is applied at the control point, which is the three-quarter-chord location for each horseshoe vortex. As a consequence of using a single chordwise horseshoe vortex, the method is restricting to wings of moderate to high aspect ratio. Although Levinsky refers to the method as a lifting-line method, the vortex model is more commonly referred to as a vortex lattice method (with a single chordwise row of horseshoe vortices) or a discrete-vortex Weissinger's method. It must be mentioned that this method differs from Prandtl's classical LLT in the implementation of the boundary condition.

In order to account for the nonlinear lift-curve slopes, the iterative technique described earlier was implemented by Piszkin and Levinsky. At each step of the iteration, the downwash computed using the $\Gamma$ distribution from the previous time step is used to compute the change in the $\Gamma$ distribution using the airfoil lift curve. This change, multiplied by a specified damping factor, $C$, is then added to the old $\Gamma$ distribution to obtain the new $\Gamma$ distribution for the next iteration. A damping factor of $C < 1$ is required to stabilize the iterations, although it results in a larger number of iterations for convergence. Unlike in the traditional LLT, where the effective section angle of attack distribution is computed as part of the solu-

tion, with the vortex model that Piszkin and Levinsky used in their method, the effective section angle distribution is not readily available. They have, however, bypassed this difficulty by defining the effective downwash angle at a section as $\alpha_{3D} - \alpha_{2D}$, where $\alpha_{3D}$ is the downwash angle at the control point resulting from the entire vortex system and $\alpha_{2D}$ is the induced angle from an infinite span bound vortex along the $c/4$ line with strength equal to that of the horseshoe vortex under consideration. From this downwash angle, they compute the effective angle of attack at every section of the wing. This formulation does not include the effects of sweep and dihedral for the effective angle of attack.[6]

Using their method, Piszkin and Levinsky found that multiple converged solutions are possible, including some that have saw-tooth type oscillations in the spanwise lift distributions. Because they were restricted to the use of 10 panels per side of the wing in their computer program, they were unable to determine whether these oscillations are present for more dense panel distributions. To avoid these oscillations, they used a switching logic that restarts the iteration procedure with an initial distribution having a zero induced $\alpha$ for any wing section found to be stalled.

With this method, the effects of different wing planform shapes and airfoil lift curves were investigated. Piszkin and Levinsky present the occurrence of lift hysteresis for increasing and decreasing $\alpha$ and the occurrence of zero-$\beta$ rolling moments at post-stall conditions. The results confirm that depending on the starting solution for the initial lift distribution for the iteration, multiple solutions are possible for the converged lift distribution for a post-stall angle of attack. Some of these lift distributions may be asymmetric even though the flight condition is exactly symmetric. The asymmetric solutions for zero $\beta$ were obtained by using a converged solution for a nonzero $\beta$ as a starting point for the iteration. Like Sears, Levinsky[6] also points out the need for a method of calculating the relative stability of the different possible solutions for the lift distribution at a given angle of attack. Finally, Levinsky[6] points out the need for an unsteady nonlinear lifting surface theory that can handle low aspect ratio wings for fighters and other such configurations, as nonlinear methods until that point were capable of handling only moderate and high aspect ratio wings. The Piszkin-Levinsky method has recently been used by Anderson[7] for aircraft high-$\alpha$ stability analysis.

Four years after Levinsky's publication, Anderson, Corda, and Van Wie[8] published a nonlinear lifting-line theory that they applied to drooped leading-edge wings below and above stall. At that time, there was considerable interest in improving the stall-spin behavior of general aviation aircraft, and part-span drooped leading-edge wings were generating interest for their benign stall characteristics. Ref. 8 provides a theoretical approach to design of such wings and presents results for $C_L$-$\alpha$ curves that extended to very high post-stall angles of attack close to 50 deg.

McCormick presents a similar, independently developed approach[9] wherein the nonlinear lifting-line theory was used to examine the loss in roll damping for a wing near stall. In both Refs. 8 and 9, no asymmetric lift distributions for symmetric flight conditions were observed even when the iterations were started with asymmetric initial lift. This observation differs from those of Sears and Levinsky.

An entirely different approach to the use of nonlinear section data was developed by Tseng and Lan.[10] While their main focus was on vortex-dominated flows on low aspect ratio fighter-type wings at high $\alpha$, they incorporated the effect of boundary-layer separation by iteratively reducing the angle of attack at each section of the wing. The reduction at any given wing section is determined by the difference between the potential flow solution and the viscous $C_l$ from the nonlinear section $C_l$-$\alpha$ curve. More recently, an approach similar to that reported in Ref. 10 was used in Ref. 11 for rapid estimation of $C_{L_{max}}$ and other high-lift characteristics for airplane configurations.

The approach described in this paper is the first part of an on-going effort aimed at developing an aerodynamic prediction method for post-stall prediction of multiple wings. This prediction method will then be used in developing flight control methods for aircraft in post-stall flight conditions. In the current research, a decambering approach was developed wherein the chordwise camber distribution at each section of the wing was reduced to account for the viscous effects at high angles of attack. The current approach has similarity with that developed in Ref. 10, but differs in the use of both the $C_l$ and $C_m$ data for the section and in the use of a two-variable function for the decambering. In addition, unlike all earlier methods, the current approach uses a multidimensional Newton iteration that accounts for the cross-coupling effects between the sections in predicting the decambering for each step in the iteration.

The subsequent discussion illustrates the decambering approach by describing its application to model a two-dimensional flow past an example airfoil. The iterative approach for three-dimensional geometries is discussed next. The results from the approach are then presented for a rectangular wing and a tapered wing at high angles of attack.

## Application to Two-Dimensional Flow

The overall objective was to arrive at a scheme for incorporating the nonlinear section lift curves in wing analysis methods such as LLT, discrete-vortex Weissinger's method, and vortex lattice methods. For this purpose, it was assumed that the two-dimensional data ($C_l$ and $C_m$ as functions of $\alpha$) for the sections

forming the wing were available from either experimental or computational results. The objective was that for the final solution of the three-dimensional flow, the $\Gamma$ distribution across the span would be consistent with the distribution of the effective $\alpha$ for each section and the $C_l$ and $C_m$ for each section would be consistent with the effective $\alpha$ for that section and the section $C_l$-$\alpha$ and $C_m$-$\alpha$ data.

In the current method, this overall objective was achieved by finding the effective reduction in the camber distribution for each section along the span. This "decambering" of the local sections was determined in an iterative fashion, more details of which are provided in the next section.

This section provides an overview of the decambering approach and illustrates the current approach by using a simple example of a two-dimensional flow past an NACA-0012 airfoil. It is illustrative to examine this approach for the two-dimensional situation first because the approach as applied to the flow past a three-dimensional finite wing will follow in the succeeding section.

The typical flow past an airfoil at small angles of attack consists of a thin boundary layer that remains attached to the surfaces of the airfoil. For these conditions, the $C_l$ and $C_m$ predicted using potential flow analysis of the airfoil camberline agrees closely with the computational and experimental results that account for viscosity.

With increasing angles of attack, the boundary layer thickens on the upper surface and finally separates, as shown in Fig. 1. It is this flow separation that causes the viscous results for $C_l$ and $C_m$ to deviate from the predictions using potential flow theory. The reason for the deviation can be related to the effective change in the airfoil camber distribution due to the boundary-layer separation. If the decambering could be accounted for, then a potential-flow prediction for the decambered airfoil would closely match the viscous $C_l$ and $C_m$ for the high-$\alpha$ flow past the original airfoil shape. This decambering idea served as the basis for the formulation of the current approach for the three-dimensional flow problem.

**Fig. 1 Flow separation from an airfoil at a high angle of attack.**

While the camber reduction due to the flow separation can be determined from computational flows, no such detailed information is available from wind tunnel results that typically provide only the $C_l$-$\alpha$ and $C_m$-$\alpha$ curves. This section discusses the approach for determining an "equivalent" camber reduction from $C_l$-$\alpha$ and $C_m$-$\alpha$ curves for an airfoil. More specifically, the effective decambering for an $\alpha$ was computed using the deviations of the viscous $C_l$ and $C_m$ from the potential flow predictions for that airfoil.

In the current method, the effective decambering for an airfoil was approximated using a function of two variables $\delta_1$ and $\delta_2$. The two linear functions shown in Figs. 2 and 3 were superposed to obtain the final decambering function. Two variables were used because the decambering was being backed out from two pieces of information: the $C_l$ and $C_m$ from the airfoil data for the $\alpha$ under consideration. This approximation will, of course, not match the actual viscous decambering, but the objective was to find an equivalent camber reduction to match the viscous $C_l$ and $C_m$ for the $\alpha$ under consideration.

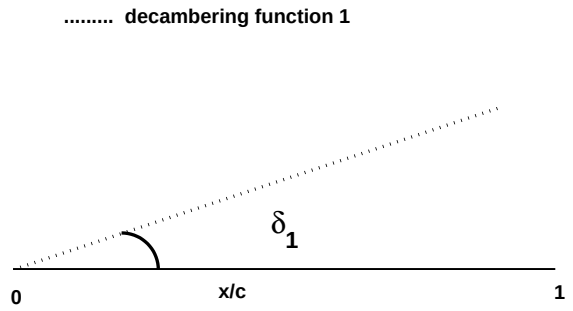


**Fig. 2 Schematic diagram of modified camberline using function 1 ($\delta_1$ is negative as shown).**

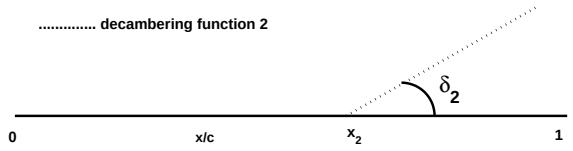


**Fig. 3 Schematic diagram of modified camberline using function 2 ($\delta_2$ is negative as shown).**

The procedure for calculating the values of $\delta_1$ and $\delta_2$ for obtaining the decambering function for an airfoil at a given $\alpha$ can be summarized as follows:

1. Evaluate the viscous $C_l$ and $C_m$ for the $\alpha$ from experimental or computational data for the airfoil.
2. Obtain the corresponding potential flow data using a lumped vortex model of the actual camberline for the airfoil.
3. Compute the difference between the viscous and the potential flow results: $\Delta C_l = (C_l)_{visc} - (C_l)_{potential}$ and $\Delta C_m = (C_m)_{visc} - (C_m)_{potential}$. These differences are shown schematically in Figs. 4 and 5 for an NACA-0012 airfoil analyzed using the XFOIL code.[12]
4. Use the difference between the viscous and the potential flow results to calculate the values of $\delta_1$ and $\delta_2$. Details of how this calculation was done follow.

The effects of $\delta_1$ and $\delta_2$ on the change in $C_l$ and $C_m$ for a given $\alpha$ can be computed reasonably well

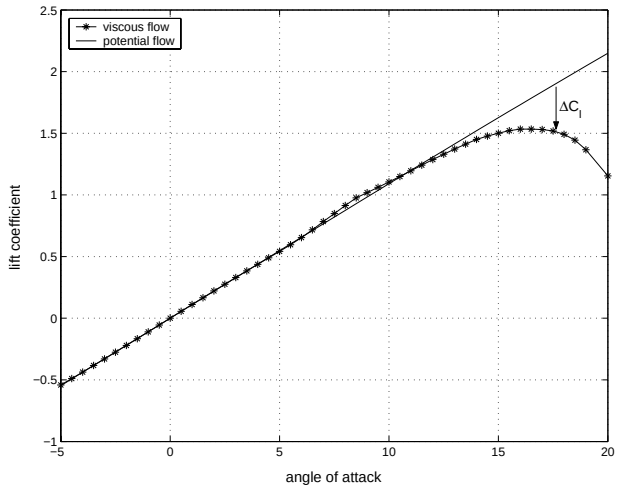


**Fig. 4** $C_l$-$\alpha$ **curves from potential and viscous methods.**

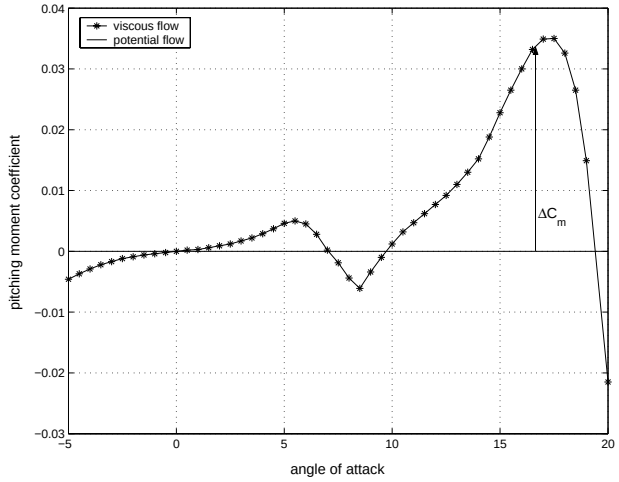


**Fig. 5** $C_m$-$\alpha$ **curves from potential and viscous methods.**

using thin airfoil theory and a three-term Fourier series approximation for a flat plate with a flap deflection.[13] These values of $\delta_1$ and $\delta_2$ in radians for given $\Delta C_l$ and $\Delta C_m$ have been derived and are presented in Eqs. 1 and 2. In these equations, $\theta_2$ is the angular location of the start point in radians for the function shown in Fig. 3 and can be expressed as shown in Eq. 3 in terms of the $x$-location of this start point, $x_2$. In the current work, $x_2$ was arbitrarily assumed to be 0.8, although any value from 0.5 to 0.9 seemed to work well.

$$\delta_2 = \frac{\Delta C_m}{\frac{1}{4}\sin 2\theta_2 - \frac{1}{2}\sin\theta_2} \tag{1}$$

$$\delta_1 = \frac{\Delta C_l - [2(\pi - \theta_2) + 2\sin\theta_2]\delta_2}{2\pi} \tag{2}$$

$$\theta_2 = cos^{-1}(1 - 2x_2); x_2 = 0.8 \tag{3}$$

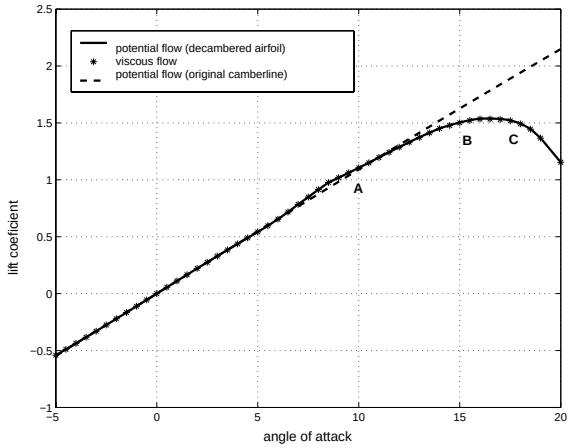


**Fig. 6** $C_l$ **curve obtained using a potential-flow method with decambering.**

To verify the effectiveness of the decambering approach, the values of $\delta_1$ and $\delta_2$ were calculated for the viscous $C_l$-$\alpha$ and $C_m$-$\alpha$ data shown earlier for the NACA-0012 airfoil in Figs. 4 and 5. These values were then applied as a correction to the flat-plate camberline for potential flow analysis of the NACA-0012 airfoil using a lumped vortex method.[13] Figure 6 shows for comparison the predicted potential flow $C_l$-$\alpha$ curve for the decambered airfoil with the viscous result from XFOIL analysis. Fig. 7 shows the comparison for the $C_m$-$\alpha$ curve with the viscous result. The agreement was seen to be very good, which verified that the two-variable decambering function can be used to model nonlinear lift as well as pitching moment curves for high angles of attack.

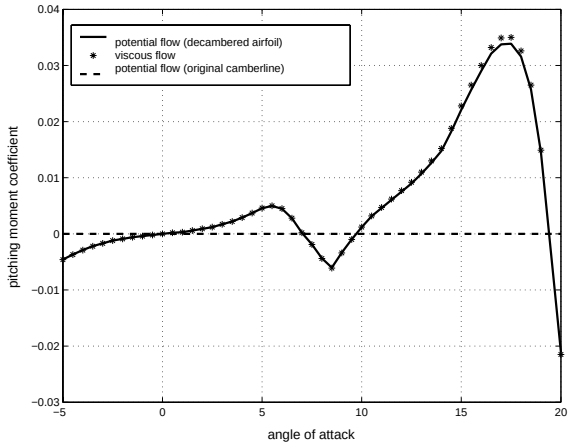


**Fig. 7** $C_m$ **curve obtained using a potential-flow method with decambering.**

To compare the approximate decambering from the two-variable function with the actual decambering from the viscous solution, comparison plots have been made for $\alpha$ of 10, 16 and 18 deg for the NACA-0012 example. The actual decambering was computed from the boundary-layer displacement thickness dis-

tributions predicted by XFOIL. Figures 8, 9, and 10 show (a) the airfoil geometry with the boundary-layer overlay and (b) the approximate and the actual decambering functions for the three angles of attack. The progressive increase in the decambering required to model the boundary-layer separation at the higher angles of attack is seen. Also seen is that the two-variable function used was a reasonable approximation of the actual decambering on the airfoil.

**a)** NACA-0012 airfoil with boundary layer at $\alpha$ of 10 deg.

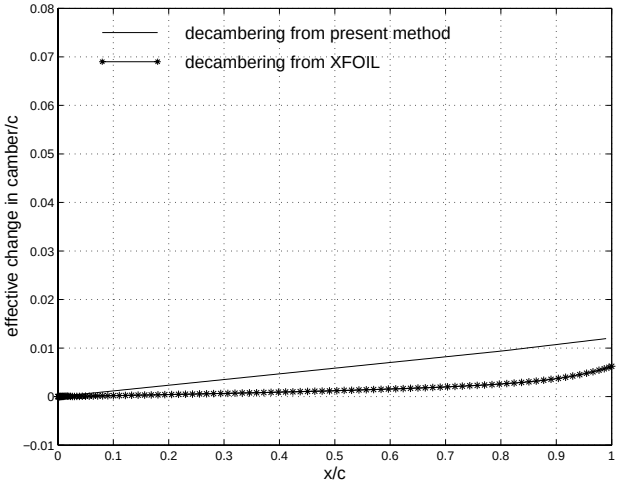


**b)** Decambering function compared with XFOIL result (y-scale shown enlarged).

**Fig. 8 Effectiveness of the decambering for $\alpha$ of 10 deg.**

**a)** NACA-0012 airfoil with boundary layer at $\alpha$ of 16 deg.

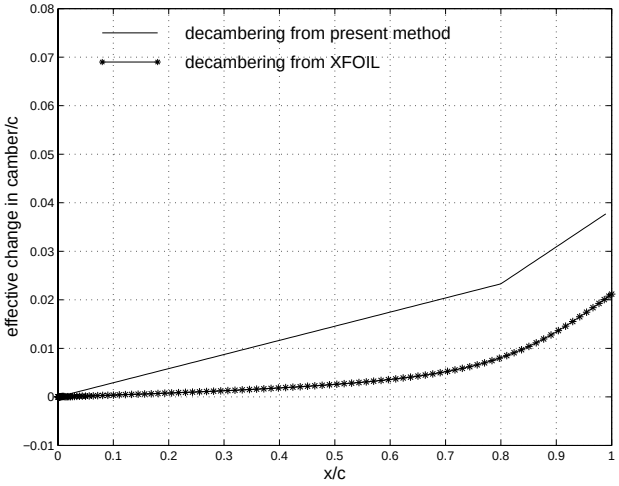


**b)** Decambering function compared with XFOIL result (y-scale shown enlarged).

**Fig. 9 Effectiveness of the decambering for $\alpha$ of 16 deg.**

**a)** NACA-0012 airfoil with boundary layer at $\alpha$ of 18 deg.

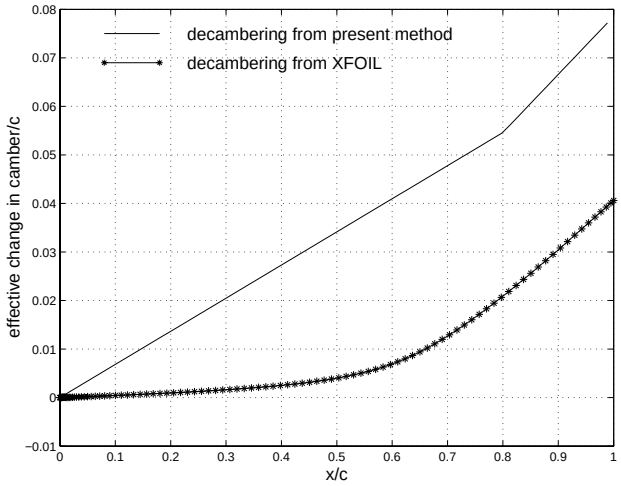


**b)** Decambering function compared with XFOIL result (y-scale shown enlarged).

**Fig. 10 Effectiveness of the decambering for $\alpha$ of 18 deg.**

This decambering approach was then extended to the finite wing analysis and the decambering at each section was evaluated in an iterative fashion.

## Application to a Finite Wing

The objective was to incorporate the two-variable decambering function in a three-dimensional analysis method such as a vortex lattice method (VLM) in an iterative fashion. In a typical VLM, the wing is divided into several spanwise and chordwise panels. Associated with each of these panels is a horseshoe vortex. In the current approach, each spanwise section $j$ (composed of a row of chordwise panels) had two variables, $\delta_{1j}$ and $\delta_{2j}$, for defining the local decambering geometry.

Unlike the two-dimensional case, where the $\delta_1$ and $\delta_2$ were selected to match the difference between the potential-flow and the viscous-flow results, in the three-dimensional case, changing a $\delta$ on one section was likely to have an effect on the neighboring sections and on sections on the downstream lifting surfaces. To account for these effects, a $2N$-dimensional Newton iteration was used to predict the $\delta_1$ and $\delta_2$ at each of the $N$ sections of the wing so that the $\Delta C_l$ and $\Delta C_m$ at these sections approached zero with an increasing number of iterations. A $2N \times 2N$ matrix equation has to be solved for each step of the Newton iteration,[14] as shown in Eq. 4.

$$\mathbf{J} \cdot \delta\mathbf{x} = -\mathbf{F} \tag{4}$$

where $\mathbf{F}$ is a $2N$-dimensional vector containing the residuals of the functions $f_i$ to be zeroed, $\delta\mathbf{x}$ is the $2N$-dimensional vector containing the corrections required to the $2N$ variables $x_i$ to bring the vector $\mathbf{F}$ closer to zero, and $\mathbf{J}$ is the $2N \times 2N$ Jacobian of the system containing the gradient information. For each step of the iteration, $\mathbf{F}$ and $\mathbf{J}$ are determined, and $\delta\mathbf{x}$ is computed using Eq. 4. The corrections are then applied to the variables to bring the residuals closer to zero. In the current scheme, the residual functions $f$ were the values of the $\Delta C_l$ and $\Delta C_m$ for each of the wing sections, and the variables $x$ were the values of $\delta_1$ and $\delta_2$ for each of the sections.

The Jacobian can be partitioned into four submatrices as shown in Eq. 5. Equations 6–9 show the elements of the four submatrices.

$$J = \begin{pmatrix} J_{l1} & J_{l2} \\ J_{m1} & J_{m2} \end{pmatrix} \tag{5}$$

$$(J_{l1})_{i,j} = \frac{\partial \Delta C_{li}}{\partial \delta_{1,j}} \tag{6}$$

$$(J_{m1})_{i,j} = \frac{\partial \Delta C_{mi}}{\partial \delta_{1,j}} \tag{7}$$

$$(J_{l2})_{i,j} = \frac{\partial \Delta C_{li}}{\partial \delta_{2,j}} \tag{8}$$

$$(J_{m2})_{i,j} = \frac{\partial \Delta C_{mi}}{\partial \delta_{2,j}} \tag{9}$$

The iteration procedure can be summarized as follows:

1. Assume starting values of $\delta_1$ and $\delta_2$ for each section of the wing.

2. Compute the wing aerodynamic characteristics using the VLM code.

3. Compute the local section effective angles of attack $\alpha_{sec}$ using the local section $(C_l)_{sec}$ and Eq. 10. It is to be noted here that in Eq. 10, the variables $\delta_1$, $\delta_2$ and $\theta_2$ are defined for a each section of the wing and are equivalent to those used earlier for the two-dimensional case in Eqs. 1, 2 and 3.

4. Compute the residuals $\Delta C_l = (C_l)_{visc} - (C_l)_{sec}$ and $\Delta C_m = (C_m)_{visc} - (C_m)_{sec}$. The $(C_l)_{visc}$ and $(C_m)_{visc}$ are obtained from the known section data for the angle of attack corresponding to $\alpha_{sec}$.

5. Calculate the Jacobian matrix for the Newton iteration.

6. Solve the matrix Eq. 4 to obtain the perturbations to $\delta_1$ and $\delta_2$ at each section and update the values of $\delta_1$ and $\delta_2$.

7. Repeat steps 2–6 until $\Delta C_l$ and $\Delta C_m$ are close to zero within a specified tolerance.

$$\alpha_{sec} = \frac{(C_l)_{sec}}{2\pi} - \delta_1 - \delta_2[1 - \frac{\theta_2}{\pi} + \frac{sin\theta_2}{\pi}] \tag{10}$$

It must be mentioned that for cases where the experimental/computational viscous data for the airfoil section does not have $C_m$, or for cases where the decambering approach is applied to an analysis method that cannot compute the section pitching moments (e.g. LLT or a discrete-vortex Weissinger's method), the decambering is modeled as a function of a single variable $\delta_1$; $\delta_2$ is assumed to be set to zero. In this case, the viscous decambering function becomes similar to the $\alpha$-reduction approach used in Refs. 10 and 11. However, in the current approach, the cross coupling between the sections was still accounted for in predicting the $\delta_1$ values for the next step. In the earlier approaches, the sections are assumed to be decoupled, and the $\delta_1$ values for each section are predicted using just the local values of the $\Delta C_l$. For this reason, it is believed that the current method will be more effective in handling situations where the section flows are closely coupled.

## Results

The iterative approach discussed in the preceding section was implemented in two different analysis methods: (1) a custom VLM code (VLM3D) designed from the outset to have the iterative approach and (2) a multiple lifting surface code *Wings*[15] based on the discrete-vortex Weissinger's method.

To illustrate the effectiveness of the method, results are presented for a high aspect ratio wing for a rectangular geometry with constant chord and zero sweep and a tapered wing geometry with taper ratio 0.3 and zero sweep. Both wings have an aspect ratio of 10. The right-side planforms for the two wings are shown in Figs. 11 and 12. The airfoil is assumed to have a lift curve that is shown in Fig. 13. This lift curve is similar to those used by Sears[3] and by Levinsky.[6]

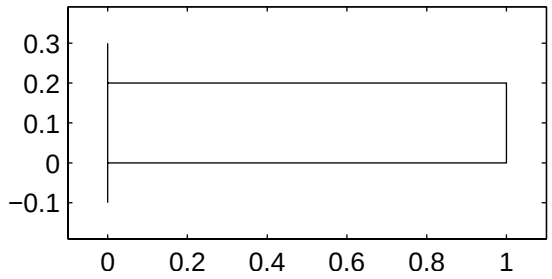


**Fig. 11 Planform of the rectangular wing (RHS shown).**

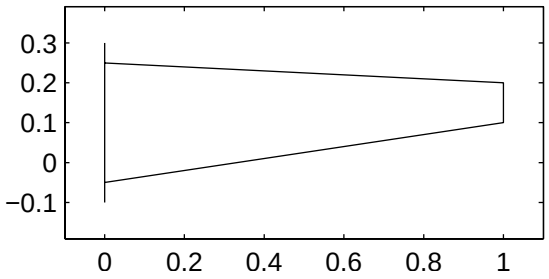


**Fig. 12 Planform of the tapered wing (RHS shown).**

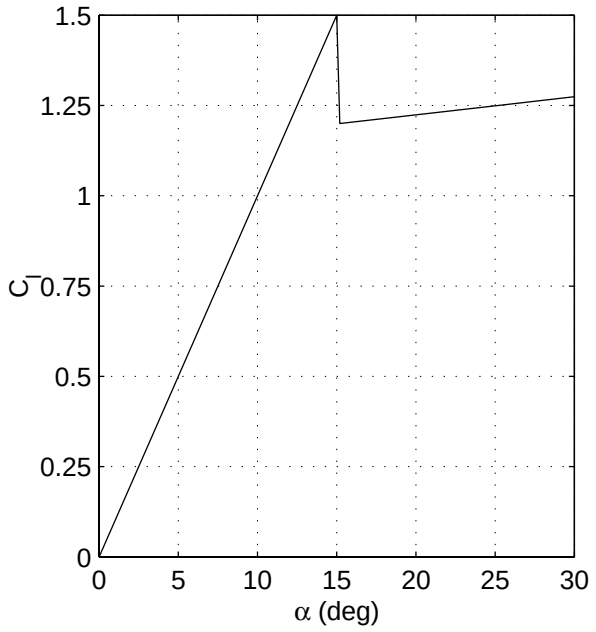


**Fig. 13 Assumed airfoil lift curve for the example wing.**

**Results from *Wings* (rectangular planform)**

Fig. 14 shows the three-dimensional $C_L$-$\alpha$ curve for the rectangular wing for both increasing and decreasing $\alpha$. Also shown is the $C_l$-$\alpha$ curve for the airfoil. For each $\alpha$ except for the first one, the starting values of $\delta_1$ were taken from the converged result for the previous $\alpha$. The hysteresis loop for post-stall condition is clearly seen confirming that for these conditions there are multiple solutions. The spanwise $C_l$ distributions are shown in Fig. 15 for both increasing and decreasing $\alpha$ for $\alpha$ values of 10, 15, 16, and 25. These values were chosen for illustrating the stall and hysteresis behavior.

From Fig. 14, it is seen that as the $\alpha$ was increased to 15.5 deg, the $C_L$ continued to increase. At these conditions, the entire wing remained unstalled as the local section $C_l$ values were less than $C_{l_{max}}$ of 1.5. This result can be confirmed by examining the increasing-$\alpha$ curves for the $C_l$ distributions in Fig. 15 for $\alpha$ of 10 and 15 deg. At $\alpha$ of 15 deg, it is seen that the inboard portion of the wing was close to stall. As the $\alpha$ was

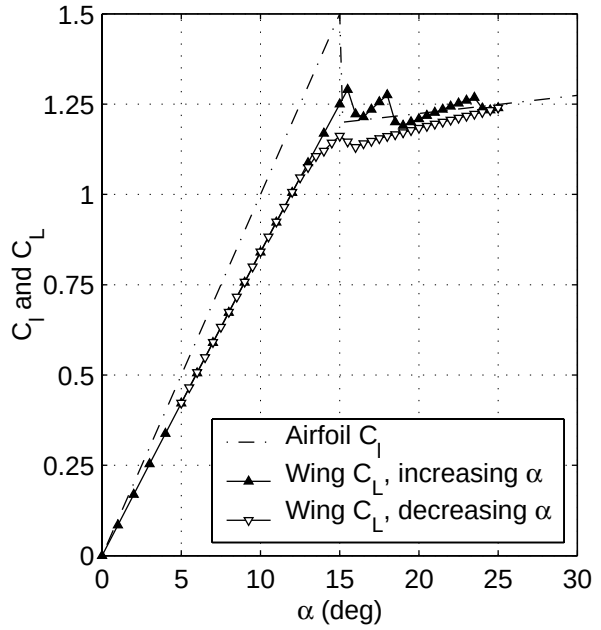


**Fig. 14 Lift curve from the *Wings* code for the rectangular wing for increasing and decreasing $\alpha$.**

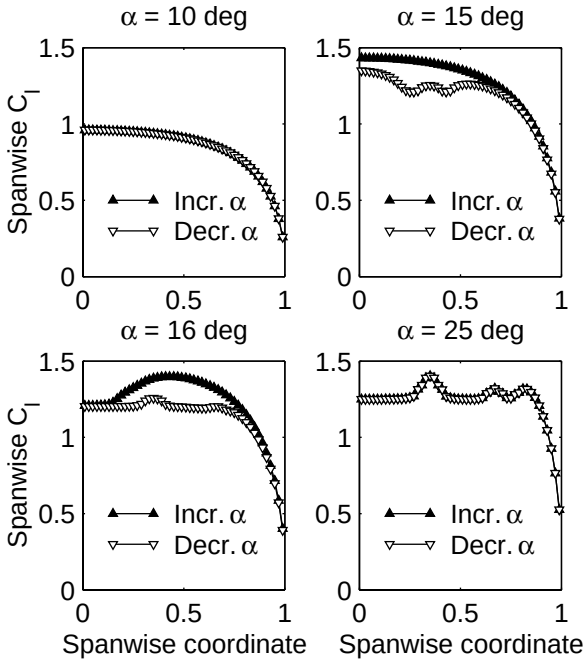


**Fig. 15 Spanwise $C_l$ distributions from the *Wings* code for the rectangular wing for increasing and decreasing $\alpha$.**

increased from 15 deg to 18 deg, the inboard portion of the wing stalled as seen in the increasing-$\alpha$ spanwise $C_l$ plot for $\alpha$ of 16 deg. As a result the $C_L$ decreased beyond wing $\alpha$ of 15.5 deg. Although the inboard portion of the wing was stalled, the $C_l$ on the outboard portion continued to increase with $\alpha$; this caused the $C_L$ to increase again between 16.5 deg and 18 deg. Beyond 18 deg, the outboard portion of the wing also

stalled, creating two stall cells on the wing. As the $\alpha$ was increased to 25 deg, almost the entire wing was stalled except for three small pockets of unstalled flow. Because almost the entire wing was stalled, the wing $C_L$ curve started coinciding with the airfoil $C_l$ curve.

When the $\alpha$ was decreased from 25 deg, the lower portion of the hysteresis loop was formed. Because the initial solutions for the iterations for the decreasing-$\alpha$ case were from stalled conditions, the $C_l$ distributions for $\alpha$ of 16 and 15 deg were different from those for the corresponding increasing-$\alpha$ plots. As the $\alpha$ was decreased to approximately 12 deg, the entire wing became unstalled and the $C_L$ curve coincided with the increasing-$\alpha$ curve.

**Results from VLM3D (rectangular planform)**

The vortex lattice method (VLM3D) code was used to analyze the wing shown in Fig. 11. The airfoil characteristics shown in Fig. 13 were used as the section data. For this analysis, 10 chordwise lattices were used. Fig. 16 shows the three-dimensional $C_L$-$\alpha$ curve for the rectangular wing obtained using the VLM3D code for increasing and decreasing $\alpha$. Also shown is the $C_l$-$\alpha$ curve for the airfoil. Although the results did not match exactly with the *Wings* code, the trends were similar. In particular, the hysteresis behavior was similar to that predicted by the *Wings* code. Fig. 17 show the spanwise distributions for the increasing-$\alpha$ and decreasing-$\alpha$ conditions at four angles of attack. These results were also similar to those seen from the *Wings* code.

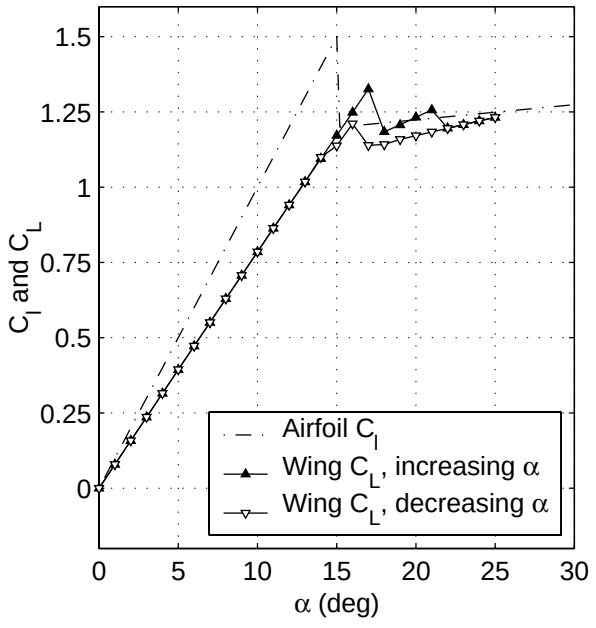


**Fig. 16 Lift curve from the VLM code for the rectangular wing for increasing and decreasing $\alpha$.**

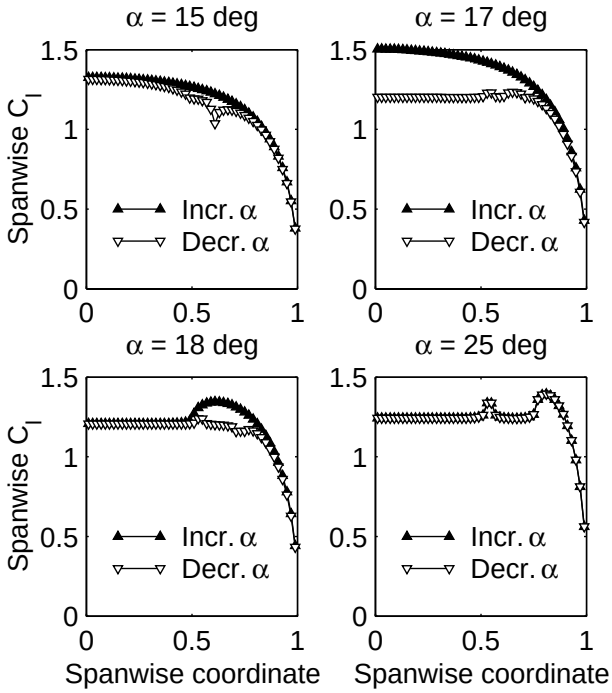


**Fig. 17 Spanwise $C_l$ distributions from the VLM code for the rectangular wing for increasing and decreasing $\alpha$.**

**Results from *Wings* (tapered planform)**

Results were obtained for the tapered wing geometry shown in Fig. 12 using the airfoil lift curve data shown in Fig. 13.

Fig. 18 shows the three-dimensional $C_L$-$\alpha$ curve for the tapered wing for increasing and decreasing $\alpha$ along with the $C_l$-$\alpha$ curve for the airfoil. The spanwise $C_l$ distributions are shown in Fig. 19 for increasing and decreasing $\alpha$ for $\alpha$ values of 10, 16, 17, and 25.

From Fig. 18, it is seen that as the $\alpha$ is increased to 16 deg, the $C_L$ continued to increase. At these conditions, the entire wing remained unstalled as the local section $C_l$ values are less than $C_{l_{max}}$ of 1.5. This result can be confirmed by examining the increasing-$\alpha$ curves for the $C_l$ distributions in Fig. 19 for $\alpha$ of 10 and 16 deg. At $\alpha$ of 16 deg, it is seen that the outboard portion of the wing is close to stall. As the $\alpha$ was increased from 16 deg to 17 deg, the outboard portion of the wing stalls as seen in the increasing-$\alpha$ spanwise $C_l$ plot for $\alpha$ of 17 deg. As the $\alpha$ was increased to 25 deg, almost the entire wing was stalled except for four small pockets of unstalled flow. These results were similar to those seen for the rectangular wing, except that the tapered wing experiences a tip stall as opposed to the root stall behavior of the rectangular wing.

**Results from VLM3D (tapered planform)**

Fig. 20 shows the three-dimensional $C_L$-$\alpha$ curve for the tapered wing for increasing and decreasing $\alpha$ along with the $C_l$-$\alpha$ curve for the airfoil. Fig. 21 show the spanwise distributions for the increasing-$\alpha$ and

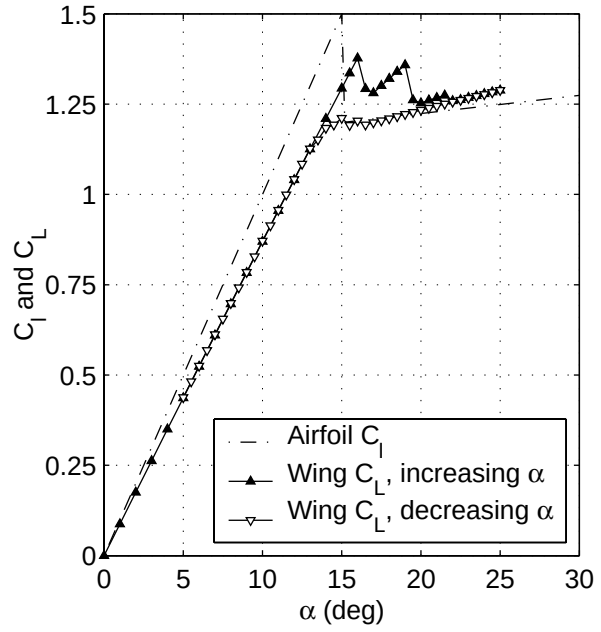


**Fig. 18 Lift curve from the *Wings* code for the tapered wing for increasing and decreasing $\alpha$.**

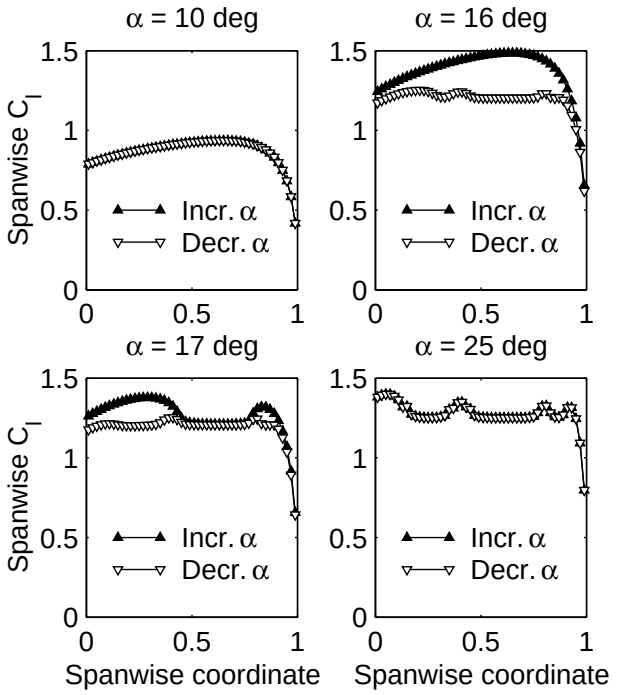


**Fig. 19 Spanwise $C_l$ distributions from the *Wings* code for the tapered wing for increasing and decreasing $\alpha$.**

decreasing-$\alpha$ conditions at four angles of attack. As with the rectangular wing, the comparison between the results from the two codes for the tapered wing were in close agreement.

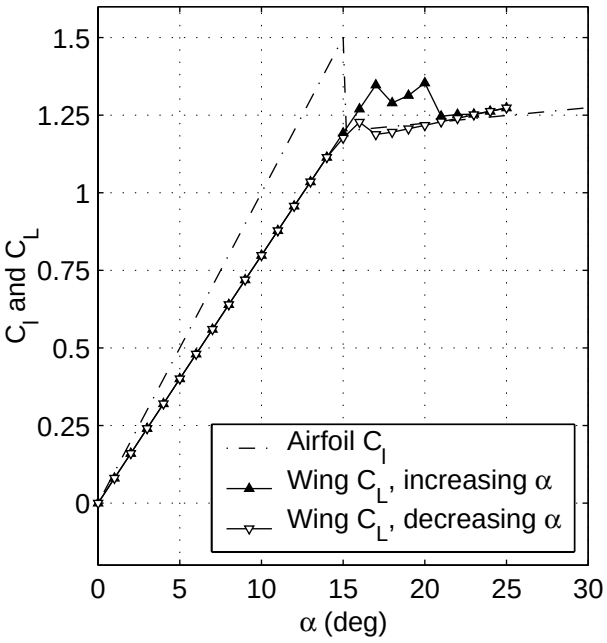


**Fig. 20 Lift curve from the VLM code for the tapered wing for increasing and decreasing $\alpha$.**

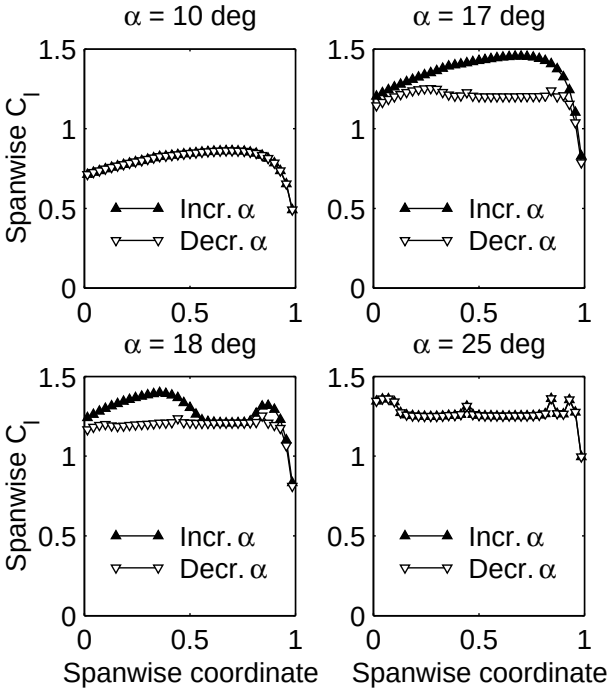


**Fig. 21 Spanwise $C_l$ distributions from the VLM code for the tapered wing for increasing and decreasing $\alpha$.**

## Conclusions

Successful prediction of near and post-stall wing aerodynamics is essential for modeling of flight vehicle stability and control at high angles of attack. Some of the potential benefits include reduction in landing distances, ability to execute evasive maneuvers, and ability to avoid loss of control when encountering severe

atmospheric turbulence and downbursts. The research presented in this paper was part of an on-going effort aimed at the development of high-$\alpha$ aerodynamic prediction methods for aircraft.

In this early part of the research, a method has been developed for stall and post-stall analysis of wings using known two-dimensional lift and moment curves for the airfoil. The method uses a decambering approach that accounts for the boundary-layer separation effects for each section of the wing in an iterative fashion. For the iteration process, a multidimensional Newton iteration was used that automatically took into account the effect of the decambering at one section on the lift at all of the other sections. The current approach also uses a two-variable decambering function that was determined by deviations in the local section $C_l$ and $C_m$ values from those predicted using potential flow. Results are presented for a rectangular wing at high angles of attack. Unlike the results in earlier work,[9] the spanwise lift distributions did not exhibit high-frequency spanwise oscillations. This improvement is believed to be due to the use of a multidimensional Newton iteration that accounted for the cross-coupling effects at every step of the iteration.

In follow-on work, the approach described in this paper will be refined. The results will be generated using the code for wing configurations for which experimental data is available. These experimental results will be used for validation of the current approach. The approach will then be extended and applied to multiple wing configurations (wing-tail and wing-canard configurations). The methods will also be extended to nonzero yaw flight conditions to examine the possibility of generating antisymmetric lift distributions at symmetric flight conditions. These methods will subsequently be used to generate aerodynamic models that will be used in a parallel, on-going effort to develop control techniques for high-$\alpha$ flight. The final aim will be to make progress in the prediction and control of aircraft at post-stall flight conditions.

## Acknowledgment

The support for the first two authors was provided under Grant NAG-1-01119 from the NASA Langley Research Center. This support is gratefully acknowledged.

## References

[1]Tani, I., "A Simple Method of Calculating the Induced Velocity of a Monoplane Wing," Rep. No. 111(vol. 9, 3), Aero. Res. Inst., Tokyo Imperial Univ., August 1934.

[2]Sivells, J. C. and Neely, R. H., "Method for Calculating Wing Characteristics by Lifting-Line Theory Using Nonlinear Section Lift Data," NACA TN 1269, April 1947.

[3]Sears, W. R., "Some Recent Developments in Airfoil Theory," *Journal of The Aeronautical Sciences*, Vol. 23, May 1956, pp. 490–499.

[4]Schairer, R. S., *Unsymmetrical Lift Distributions on a Stalled Monoplane Wing*, Master's thesis, California Institute of Technology, 1939.

[5]Piszkin, S. T. and Levinsky, E. S., "Nonlinear Lifting Line Theory for Predicting Stalling Instabilities on Wings of Moderate Aspect Ratio," Tech. rep., General Dynamics Convair Report CASD-NSC-76-001, June 1976.

[6]Levinsky, E. S., "Theory of Wing Span Loading Instabilities Near Stall," AGARD Conference Proceedings No. 204, September 1976.

[7]Anderson, M. R., "Aerodynamic Modeling for Global Stability Analysis," AIAA Paper 2002-4805, August 2002.

[8]Anderson, J. D., Corda, S., and VanWie, D. M., "Numerical Lifting Line Theory Applied to Drooped Leading-Edge Wings Below and Above Stall," *Journal of Aircraft*, Vol. 17, No. 12, 1980, pp. 898–904.

[9]McCormick, B. W., "An Iterative Non-Linear Lifting Line Model for Wings with Unsymmetrical Stall," *SAE Transactions Paper No. 891020*, 1989, pp. 91–98.

[10]Tseng, J. B. and Lan, C. E., "Calculation of Aerodynamic Characteristics of Airplane Configurations at High Angles of Attack," NASA CR 4182, 1988.

[11]van Dam, C. P., Kam, J. C. V., and Paris, J. K., "Design-Oriented High-Lift Methodology for General Aviation and Civil Transport Aircraft," *Journal of Aircraft*, Vol. 38, No. 6, November–December 2001, pp. 1076–1084.

[12]Drela, M., "XFOIL: An Analysis and Design System for Low Reynolds Number Airfoils," *Low Reynolds Number Aerodynamics*, edited by T. J. Mueller, Vol. 54 of *Lecture Notes in Engineering*, Springer-Verlag, New York, June 1989, pp. 1–12.

[13]Katz, J. and Plotkin, A., *Low-Speed Aerodynamics From Wing Theory to Panel Methods*, McGraw-Hill, Inc., 1991.

[14]Press, W. H., Teukolsky, S. A., Vetterling, W. T., and Flannery, B. P., *Numerical Recipes in Fortran — The Art of Scientific Computing*, Cambridge University Press, New York, 2nd ed., 1992.

[15]Gopalarathnam, A. and McAvoy, C. W., "Effect of Airfoil Characteristics on Aircraft Performance," *Journal of Aircraft*, Vol. 39, No. 3, May–June 2002, pp. 427–433.